

Equilibrium Morphology of Face-Centered Cubic Gold Nanoparticles >3 nm and the Shape Changes Induced by Temperature

A. S. Barnard,^{*,†,‡} X. M. Lin,^{†,‡,§} and L. A. Curtiss^{‡,§}

Center for Nanoscale Materials, Materials Science Division, and Chemistry Division,
Argonne National Laboratory, 9700 South Cass Avenue, Argonne, Illinois 60439

Received: August 2, 2005; In Final Form: October 24, 2005

Many of the unique properties of metallic nanoparticles are determined not only by their finite size but also by their shape, defined by the crystallographic orientation of the surface facets. These surfaces (and therefore the nanoparticles themselves) may differ in a number of ways, including surface atom densities, electronic structure, bonding, chemical reactivities, and thermodynamic properties. In the case of gold, it is known that the melting temperature of nanoparticles strongly depends on the crystal size and that the shape may alter considerably (and yet somewhat unpredictably) during annealing. In this work we use first principle calculations and a thermodynamic model to investigate the morphology of gold nanoparticles in the range 3–100 nm. The results predict that the equilibrium shape of gold nanoparticles is a modified truncated octahedron and that the (size-dependent) melting of such particles is preceded by a significant change in the nanoparticle's morphology.

1. Introduction

Metallic nanoparticles containing tens to thousands of atoms are attracting considerable interest, largely because the transition from molecule-like behavior to bulk properties occurs in this size regime. Research activities in this area have mainly focused on the size-dependent physical properties,^{1,2} motivated by possible applications as catalysts as well as electrical and optical components in nanodevices.^{3–6} However, the unique properties of metallic nanoparticles are determined not only by their finite size (resulting in a large fraction of atoms occupying the surfaces) but also on the particle shape, defined by the relative area of different surface facets.⁷ For instance, the plasmon excitation of gold or silver nanorods can span the entire visible wavelength by simply changing their aspect ratio.⁸ Compared with “spherical” particles, the rod-shaped particles show a much greater electromagnetic enhancement for molecular surface Raman scattering.^{9,10} Recent syntheses using a cationic surfactant cetyltrimethylammonium bromide (CTAB) have generated not only nanorods¹¹ but also bipod and tripod structures that intuitively seem energetically unfavorable.¹² These developments have prompted renewed interest in understanding the energy and stress of different crystal surfaces and how the surface ligand binds to different facets.

In addition to surface chemistry, thermodynamic considerations are also known to play an important role in governing the morphology of gold nanoparticles. Although many bulk metals have the face-centered cubic (fcc) structure, small clusters (typically less than 3 nm) of the same materials may exhibit various structural and morphological modifications. Metallic clusters have been observed as cuboctahedral fcc structures,¹³ singly or multiply twinned fcc structures,^{14,15} twinned hexagonal

close-packed (hcp) structures,¹⁶ icosahedral and truncated icosahedral (I_h) structures,^{15,17–20} as well as the Marks decahedral^{17,18} and truncated decahedral (D_h) structures.^{17,18}

The majority of previous computational (and theoretical) studies on gold structures >3 nm in size have focused on the icosahedral and decahedral particles, since these have been found to be the lower energy morphology for small clusters (<3 nm).^{21–25} In the case of the icosahedral clusters, such studies have indicated that as the size of the cluster increases, the stability of the icosahedral structures decreases significantly,^{21,26,27} due to accumulated strain energy.^{22,23,25} In the case of decahedral particles, computational studies have shown that gold nanoclusters in the range 1–2 nm are more likely to form in three discrete cluster sizes belonging to the truncated Marks decahedral motif (with particular truncations), than any other shape.^{22,25} These and numerous other computational studies of decahedral and icosahedral gold nanostructure have been reviewed in ref 28.

Samples of larger gold nanoparticles (over ~5 nm) are known to have a far fewer fraction of particles with icosahedral or decahedral shapes, based on observations of a number of studies.^{13,29,30} However the exact shape of these particles, under either equilibrium or nonequilibrium conditions (such as during annealing), is currently unknown. To investigate this problem, we have used a multiscale thermodynamic model³³ based on the Gibbs free energy of (arbitrary) nanoparticles as a function of size and shape to systematically compare various possible (nonequilibrium) shapes and to determine the minimum energy morphology of fcc gold nanoparticles for sizes ranging from 3 to 20 nm. The advantages of this type of thermodynamic modeling include the ability to compare nonequilibrium shapes, to optimize the morphology with respect to experimentally relevant parameters such as temperature, and to consider large nanoparticles at sizes traditionally inaccessible to all but atomistic level simulations. This study therefore represents the first investigation of gold nanoparticles at experimentally relevant sizes, based on electronic structure.

* Current address: Department of Materials, University of Oxford, Parks Road, Oxford, OX1 3PH, U.K. Current e-mail: amanda.barnard@materials.ox.ac.uk.

† Center for Nanoscale Materials.

‡ Materials Science Division.

§ Chemistry Division.

As input into the model, the surface free energies and the surface stresses for the {111} and {100} surfaces have been calculated using scalar relativistic first principles methods. Following the examination of the equilibrium nanomorphology, we have used the model to investigate the effect of temperature on the shape of gold nanoparticles in the range 4–12 nm. It is known that the melting temperature of gold nanoparticles strongly depends on size, with the melting point of ~2.5 nm particles being as much as ~40% lower than that of (macroscopic) bulk gold.³⁵ Our results predict that the size-dependent melting of the (equilibrium-shaped) fcc nanoparticles is preceded by a dramatic change in shape, the degree of which increases with increasing particle size. Using the shape versus temperature results in combination with the shape observed in real nanoparticles under the electron microscope, we have made an estimate of the temperature at which such nanoparticles are annealed due to exposure to the electron beams during imaging.

Before embarking upon a theoretical analysis of the shape of large nanoparticles, it is first important to gain an appreciation of the shapes observed in real specimens. Previous experimental studies^{13,29,30,37} have tended to assign the truncated octahedral or cuboctahedral motif, without providing a detailed description of the exact fraction of {111} to {100} surface area. In section 2 we have analyzed the shapes of large (~6 nm) particles from experiments. This information is particularly important here, if we are to accurately model the shape transitions of fcc gold nanoparticles approximately 3–20 nm in size.

2. Experimental Background

Synthesis of highly monodispersed noble metal nanoparticles is well developed. We adopted a digestive ripening procedure to synthesize dodecanethiol ligated nanoparticles.³⁶ This procedure yields highly monodispersed particles for each reaction with the standard particle size deviation <5%. From batch to batch, the size varies from 5 to 8 nm. We used high-resolution transmission electron microscopy (HRTEM) to examine the morphology of the particles, because it is much less ambiguous compared with techniques used to characterize small clusters, such as powder diffraction and pair distribution analysis.³⁷ Figure 1 shows a HRTEM image of 8 nm gold nanoparticles, taken with a JEM-4000EXII high-resolution electron microscope at 400 keV accelerating voltage and 1.2 M magnification. The nanoparticles have been washed repeatedly prior to being dissolved in toluene and deposited on the TEM grid, so that the amount of ligand molecules on the nanoparticle surfaces has been minimized. Careful examination of these images shows that about one-third of the particles either contain a single twin plane or are decahedral. The remaining two-thirds are single fcc structured nanoparticles, some of which appear superficially “spherical” in shape and others exhibiting some degree of faceting.

To elucidate more precisely the shape of these thiol-deficient gold nanoparticles, we have used an empirical shape-matching technique, which employs a set of eight candidate structures with varying morphology. The exact shape of each candidate structure depends on the degree of “truncation” in the $\langle 111 \rangle$ direction, beginning with an octahedron and ending with a cuboctahedron. The *set* was constructed by incrementally increasing this truncation or, alternatively, incrementally decreasing the {111} surface area (from 100% {111} to ~40% {111}). To determine the shapes of real nanoparticles, each of the candidate structures was rotated to match the orientation of a given nanoparticle HRTEM image. To do this we adopted a simplified model which projects the candidate structures on the

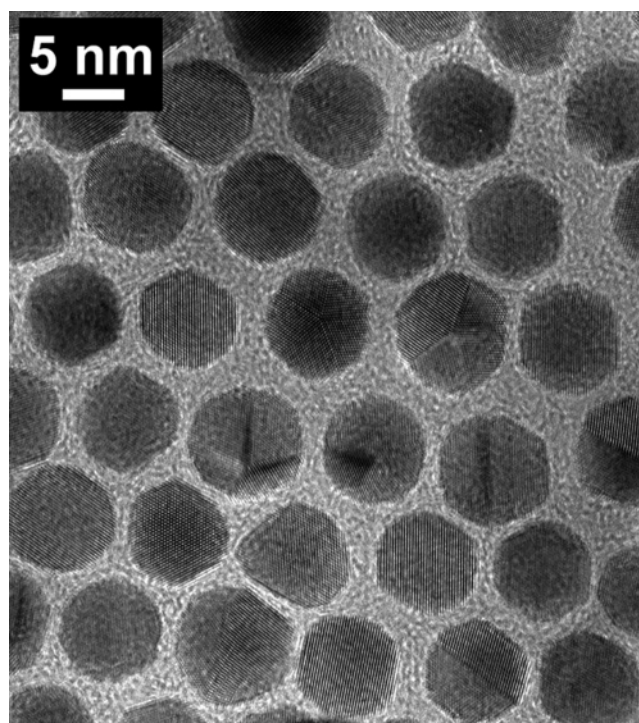


Figure 1. HRTEM image of 8 nm gold nanoparticles, synthesized using a digestive ripening technique with dodecanethiol as ligand.

two-dimensional detector. Only the outline of the nanoparticle shape and visible atomic lattices are taken into account without detailed analysis of the phase contrast. The projection is then overlapped with real HRTEM images to select the candidate structure that best reproduced the cross sectional outline of the particle. This candidate structure was then assigned to the particle as the morphology-of-best-fit. This procedure was repeated for HRTEM images of 50 independent nanoparticles, some examples of which are given in Figure 2.

Following the analysis outlined above, we found the fcc gold nanoparticles in our sample have truncated-octahedral motif and the crystal surface is dominated by {111} and {100} forms. In fact, even the more “spherical”-looking nanoparticles, such as the example shown in Figure 2d, may be described by a truncated octahedron. Statistically, the matching study revealed only a relatively small variation in the morphology of the nanoparticles, with a normal distribution centered around 77% {111} (23% {100}), with a width of 7.5% and a standard error of 1.9%. These results are in agreement with the experimental results of gold nanoparticles with fcc form in a similar size range^{13,29,30} and computational studies predicting a crossover from decahedra to fcc happen at the 500 atoms range.^{22,31} However, they are in sharp contrast with experimental results from Koga and Sugawara,³² in which icosahedron and decahedron are the dominant morphologies. It has been proposed, in the latter case, the formation of icosahedra is due to a kinetic trapping effect.²⁸ In comparison, our sample prepared through a digestive ripening process appears to exhibit a morphology much closer to the thermodynamically equilibrium shape.

3. Methodology

3.1. Theoretical. The multiscale thermodynamic model³³ mentioned above is based on a summation of the Gibbs free energy G_x^{total} of a nanoparticle of material x ($x = \text{Au}$ in this current study). In the truncated version of the model used here, the energetic contribution from edges and corners have been

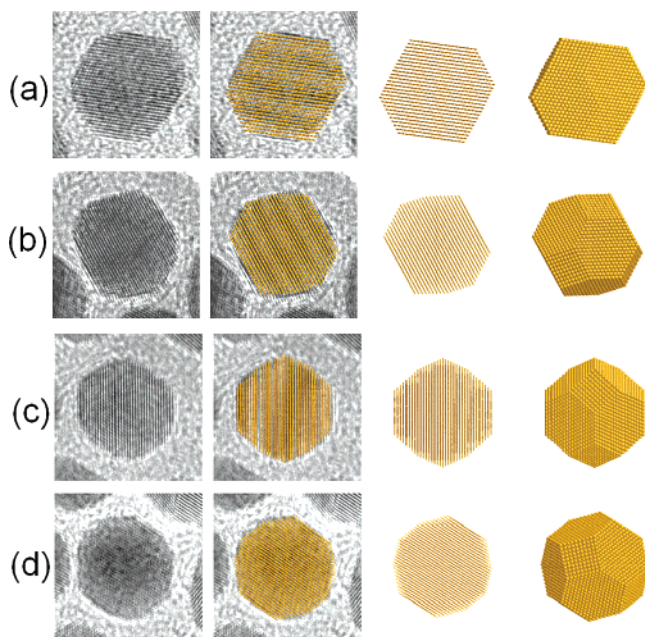


Figure 2. Examples (a–d) of the empirical shape-matching technique used to estimate the morphology of gold nanoparticles observed in HRTEM. The HRTEM image is shown to the left, and the final candidate structure assigned as the morphology-of-best-fit is shown to the right. The center columns show the projection of the candidate structure (center right) and an overlay of this projection with the HRTEM image (center left) to illustrate the matching of the lattice fringes and cross sectional outline.

ignored. A consequence of this is that results will only be valid for nanoparticles over ~ 3 nm in diameter³⁴ (since below this size the latter effects become significant and must be included); however, calculation of a complete set of these parameters is more computationally expensive than the explicit consideration of isolated < 3 nm structures (which will be reported elsewhere). More information on the operating range of applicability and testing of this model may be found in refs 33 and 34.

Therefore, for the purposes of studying gold nanocrystals > 3 nm in size, G_x^{total} is described by a sum of contributions from the nanoparticle bulk and surfaces, such that

$$G_x^{\text{total}} = G_x^{\text{bulk}} + G_x^{\text{surface}} \quad (1)$$

This is then further defined in terms of the surface energy γ_{xi} for each crystallographic surface i , weighted by the factors f_i (where $\sum_i f_i = 1$). Hence

$$G_x^{\text{total}} = \Delta_f G_x^0 + \frac{M}{\rho_x} (1 - e) [q \sum_i f_i \gamma_{xi}] \quad (2)$$

where $\Delta_f G_x^0$ is the standard free energy of formation of the bulk (macroscopic) material (which for gold is zero by definition), M is the molar mass, ρ_x is the density, and e is the volume dilation induced by the surface stress. In general, the surface-to-volume ratio q and the weighting factors f_i must be calculated explicitly for each shape and the facets therein. In this model the size dependence is introduced by the surface-to-volume ratio q and the reduction of e as the crystal increases in size. The shape dependence is also introduced by q , as well as the weighted sums of the surface energies and the surface stresses.³³

It has previously been shown³³ that the Laplace–Young equation is suitable for approximating the volume dilation of

faceted nanoparticles.³³ Therefore, the volume dilation due to the surface stress, with the bulk modulus B_0 , is defined as

$$e = \frac{2 \sum_i f_i \sigma_{xi}}{B_0 R} \quad (3)$$

where σ_{xi} is the surface stress of the particular crystallographic surface i . Although the overall affect of e is small, inclusion of this term is particularly important, since it has been reported experimentally that small (~ 4 nm) gold nanoparticles exhibit a lattice contraction, resulting in lattice parameters smaller than that of bulk gold.³⁷ Therefore, this model requires explicit determination of the values of γ_{xi} and σ_{xi} for all surfaces i of interest (along with the value of B_0).

As mentioned above two surfaces have been found to be important, so that we have $i = (111)$ and (100) . Since the surfaces of gold are nonpolar, this is equivalent to $i = \{111\}$ and $\{100\}$. These surfaces were modeled using 2×2 (surface) supercells consisting of nine and eight atomic layers perpendicular to the desired surface (with a total $N = 108$ and 64 Au atoms), respectively. Periodic boundary conditions are applied in all three Cartesian directions, and the surfaces are exposed via an additional 10 \AA of vacuum space. With these structures, the total energy for the surface slabs (E_N^{slab}) was calculated, using the methods outlined in section 3.2. A value for the bulk energy per atom (E^{bulk}) was also obtained from separate supercell calculations of larger sizes but the same computational conditions. The surface free energies γ_{xi} were then obtained (at $T = 0$) from E^{bulk} and E_N^{slab} using the expressions

$$\gamma_{xi} = \frac{G_x}{A_i} \quad (4)$$

$$G_x = \frac{1}{2} (E_N^{\text{slab}} - N E^{\text{bulk}}) \quad (5)$$

where G_x is the free energy of the slab, A_i is the area of a surface of the slab (in orientations $i = (111)$ and (100)), and N is the number of atoms in the supercell of the slab.

Similarly, the value of σ_{xi} was obtained by applying a two-dimensional dilation³⁹ to the slab in the plane of the surface and calculating the free energy G_x as indicated in eq 5. At each dilation the change in free energy (ΔG_x) was determined for a set of area dilations (ΔA_i). When these results were plotted, an estimate of the surface stress was obtained from the expansion, as described in ref 39.

The value of B_0 has been determined by calculating the energy of a 108 atom bulk (periodic) supercell for a number of volume dilations ($\pm 1\%$ to $\pm 5\%$) and then fitting the results to the Vinet equation of state.⁴⁰ The final values of $B_0 = 157 \pm 1.9$ GPa and $B'_0 = 4 \pm 0.3$ GPa are in reasonable agreement with the experimental values of 167 and 5.5 GPa measured by Heinz and Jeanloz⁴¹ and $B_0 = 167$ GPa measured by Holzapfel et al.⁴²

3.2. Computational. In determination of γ_{xi} , σ_{xi} , and B_0 , the calculations were undertaken from first principles using density functional theory (DFT) within the generalized-gradient approximation (GGA), with the exchange-correlation functional of Perdew and Wang (PW91).⁴³ This has been implemented via the Vienna ab initio Simulation Package (VASP)^{44,45} which utilizes an iterative self-consistent scheme to solve the Kohn–Sham equations using an optimized charge-density mixing routine. Each of the bulk and slab structures were fully relaxed, prior to the calculation of the total energies, using a $4 \times 4 \times 8$

and $4 \times 4 \times 1$ Monkhorst–Pack k-point mesh, respectively. The electronic relaxation technique used here is an efficient matrix-diagonalization routine based on a sequential band-by-band residual minimization method of single-electron energies,^{46,47} with direct inversion in the iterative subspace, whereas the ionic relaxation involves minimization of the Hellmann–Feynman forces. This technique has been shown to give good results for gold in the past.³⁸

The initial relaxations and the following static single point energy calculations were performed using the projected augmented wave (PAW) potentials,^{48,49} with a plane-wave basis cutoff of 250 and 350 eV (respectively), to an energy convergence of 10^{-4} eV. In all of the calculations we have included relativistic effects. The PAW potentials are generated relativistically (including mass velocity and Darwin terms), so that the radial wave functions are solutions of the scalar relativistic radial equation. In addition to this, spin polarization and spin–orbit interaction (SOI) were included in the all-electron part of the PAW Hamiltonian, and the interpolation formula proposed by Vosko, Wilk, and Nusair⁵⁰ was used for the correlation part of the exchange correlation functional. This procedure ensures that the spin directions couple to the crystalline structure.

4. Results and Discussion

In the case of the (111) surface, a surface energy of $\gamma_{\text{Au}(111)} = 0.523 \text{ J/m}^2$ was calculated. This is in good agreement with the values of 0.487 J/m^2 calculated by Needs and Mansfield using DFT LDA with scalar relativistic corrections,⁵¹ 0.513 J/m^2 calculated by Vitos et al. using full charge density linear muffin-tin orbitals (LMTO) in the atomic sphere approximation (ASA) without relativistic corrections,⁵² 0.421 J/m^2 calculated by Galanakis et al. using the full-potential linearized augmented plane wave method (FLAPW) and 0.522 J/m^2 using the full-potential screened Korringa–Kohn–Rostoker method (FKKR) with scalar relativistic corrections,⁵³ and 0.655 J/m^2 calculated by Kollár et al. using self-consistent exact muffin-tin orbitals (EMTO).³⁹ Similarly, the surface stress of $\sigma_{\text{Au}(111)} = 1.084 \text{ J/m}^2$ calculated for the (111) surface is in good agreement with the previously reported values of 1.080^{51} and 0.999 J/m^2 ³⁹ and the experimental values of 1.198 and 1.242 J/m^2 measured by Solliard et al.⁵⁴

In the case of the (100) surface, there have been comparatively fewer studies undertaken to compare with our calculated values of $\gamma_{\text{Au}(100)} = 0.606 \text{ J/m}^2$ and $\sigma_{\text{Au}(100)} = 1.174 \text{ J/m}^2$, respectively. The result for $\gamma_{\text{Au}(100)}$ is in good agreement with the calculated values of 0.660 J/m^2 (using LMTO),⁵² 0.499 J/m^2 (using FLAPW)⁵³ and 0.616 J/m^2 (using FKKR).⁵³ Note that surface energy anisotropy, described by $(\gamma_{\text{Au}(100)} - \gamma_{\text{Au}(111)})/\gamma_{\text{Au}(111)}$, computes to be 15.76%, in excellent agreement with the experimental value of 15.2 ± 0.9 measured by Flüeli and Borel at 750 K.⁵⁵

With these calculated values for $\gamma_{\text{Au}(111)}$, $\gamma_{\text{Au}(100)}$, $\sigma_{\text{Au}(111)}$, and $\sigma_{\text{Au}(100)}$ (along with $B_0 = 157 \text{ GPa}$), as input for the model given in eq 2, a comparison has been made of the energetics of gold nanoparticles of different “geometrically ideal” shapes. These shapes include a cube (terminated completely by {100} surfaces), a truncated cube, a cuboctahedron, a truncated octahedron, and an octahedron (terminated completely by {111} surfaces); as illustrated in parts a–e of Figure 3, respectively.

It might be intuitively expected that, since the {111} surfaces have a lower surface free energy, the octahedron would be the lowest energy shape, followed by the truncated octahedron, cuboctahedron, truncated cube, and then cube (with the G_x^{total} increasing with increasing degree of {100} surface area);

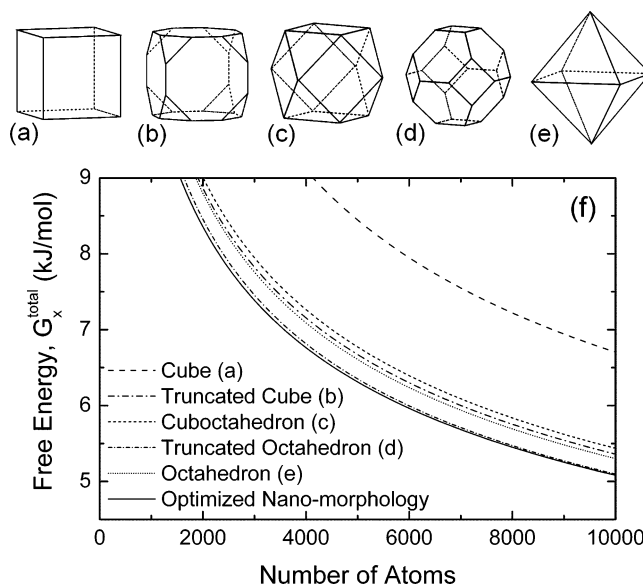


Figure 3. Comparison of the energetics of gold nanoparticles of different “geometrically ideal” shapes including a cube (a), a truncated cube (b), a cuboctahedron (c), a truncated octahedron (d), and an octahedron (e). The relative energy, along with the optimized nanoscale morphology, is shown as a function of the number of atoms in (f).

however this was not found to be the case. The results of this comparison (shown at the bottom of Figure 3) revealed that the truncated octahedron (d) is most favorable among these shapes. This is followed by the octahedron (e), truncated cube (b), cuboctahedron (c), and cube (a), respectively.

This order of morphologies results from the interplay between $\sum f_i \gamma_{xi}$ and the surface-to-volume ratio q . The cube (which is by far the highest energy shape) has the lowest relative value of q but is terminated by higher energy surfaces. By truncating the corners in the $\langle 111 \rangle$ directions to form the truncated cube, q is decreased slightly (relative to a cube), and $\sum f_i \gamma_{xi}$ decreases (due to the introduction of a some lower energy {111} surface area), resulting in a lower energy shape. Further truncation in the $\langle 111 \rangle$ directions yields a cuboctahedron, with a lower $\sum f_i \gamma_{xi}$, but this is countered by an increase in q (making the contribution from G_x^{surface} to G_x^{total} greater), resulting in a higher energy shape. In the case of the truncated octahedron, the balance between q and $\sum f_i \gamma_{xi}$ is optimal (resulting in the lowest energy shape), and for the octahedron the lowest value for $\sum f_i \gamma_{xi}$ is countered by the highest relative value of q , giving a slightly higher G_x^{total} .

Referring back to section 2 and the shape matching of the HRTEM images, the results of this comparison are not unexpected. The shape of the real specimens was estimated to be truncated octahedral with approximately 77% {111} surface area. This is very close to the ideal truncated octahedron used in the comparison above, which has 76% {111} surface area.

4.1. Optimizing Nanomorphology. The standard method for determining the equilibrium morphology of a material is to generate the Wulff construction⁵⁶ using the surface energies. However, as the Wulff construction does not take into account the effects of surface stress and the desire for nanoparticles to minimize the total surface-to-volume ratio, it is possible that the morphologies of nanoparticles may deviate from the Wulff shape. Using the model described above, we have investigated this possibility by optimizing the nanoparticle shape, as a function of size. Figure 3 includes G_x^{total} for a shape referred to as the “optimized nanomorphology”, which is lowest in energy

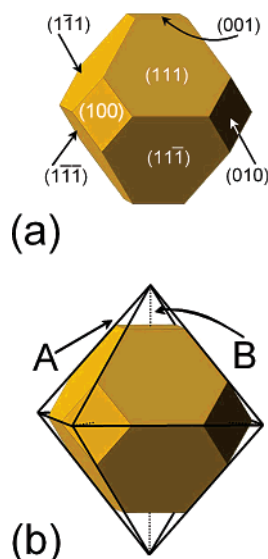


Figure 4. The Wulff construction (top) as predicted by the surface energies calculated using first principles scalar relativistic methods and schematic (bottom) showing the definition of the geometric parameters **A** (solid line) and **B** (dotted line) used for the optimization of this shape with respect to size or temperature.

for less than approximately 7000 atoms. The method used to determine this shape (as a function of size) is as follows.

Beginning with the Wulff construction as the initial case (as shown in Figure 4a), the morphology of the gold nanoparticles was defined in terms of two independent length parameters **A** and **B**. In this case the side of the {111} form has been denoted **A**, and the vector in the <111> direction is denoted **B**, as indicated in Figure 4b. The degree of truncation may therefore be described by the size of **B** with respect to **A** (where $0 \leq \mathbf{B} \leq \sqrt{2}\mathbf{A}/3$). When **B** = 0, the shape is an octahedron, when **B** = $\sqrt{2}\mathbf{A}/4$, the shape is a cuboctahedron, and when **B** = $\sqrt{2}\mathbf{A}/3$, the shape is a cube.

By defining all the geometric parameters such as the volume and surface area of the various facets in terms of the ratio **B/A**, the total free energy was minimized with respect to this new variable. The numerical minimization was performed using a conjugate gradient scheme. At small sizes (less than 20 nm) the model predicts a deviation of the **B/A** from that predicted by the Wulff construction. For particles of 3 nm in size, a ratio of **B/A** = 0.167 is predicted (89.6% {111}), for 6 nm particles, **B/A** = 0.163 (90.2% {111}), and for 9 nm particles, **B/A** = 0.161 (90.3% {111}). This converges rapidly to that of **B/A** = 0.160 predicted by the Wulff construction (90.5% {111}), becoming effectively equal at a size of 20 nm. Although this effect is very small, it is none the less a consequence of the nanoscale, due to the need for small particles to minimize the total surface stress (leading to ϵ) and the total surface-to-volume q , as well as the total surface energy. In this regime, a reduction in q (even at a cost of higher $\sum_{i,j} \gamma_{ij}$), may lower the contribution of $G_{\text{surface}}^{\text{surface}}$ to the total free energy of the particle, resulting in a shape that is lower in energy than the Wulff construction.

An important point to note here is that the fraction of {111} surface area predicted for the optimized nanomorphology and the macroscopic Wulff shape (~90%) is not the same as that determined via the shape matching in section 2 (~77%). This apparent discrepancy can be easily explained when we consider the fact that the nanoparticles in the electron microscope are not at zero temperature. The nanoparticles are heated by the electron beam and may (as a result) adopt a more nonequilibrium shape (at elevated temperatures). The same can be said for other

types of irradiation used to probe the morphology of gold, and this may account for the observation of the (nonequilibrium) cuboctahedral shape in some experiments.³⁷

4.2. Temperature-Induced Changes in Nanomorphology.

In general, the structural (and morphological) instability of gold nanoparticles under electron irradiation (due to heat imparted to the sample by the beam) has been known for some time⁵⁷ and has been examined in some detail.^{13,58} Similarly, recent studies have begun to investigate the morphological changes in larger (>10 nm) gold nanoparticles under optical irradiation.^{59,60} Link et al.⁵⁹ performed a series of measurements, varying the excitation and output power of an amplified femtosecond laser system (100 fs pulses). During the experiments the shapes of gold nanorods were found to change (in addition to some fragmentation into nanodots). The final shape of irradiation products was found to be highly dependent on the energy and width of the laser pulse.⁵⁹ In the study undertaken by Inasawa et al.,⁶⁰ the shape of large (~38 nm) gold colloidal nanoparticles was found to undergo a shape transformation from “ellipsoidal” to “spherical” when exposed to a single laser pulse (30 ps pulse width). This transformation occurred at approximately 940 °C, some 124 °C below the particle melting point (of 1064 °C).

Therefore, it is not surprising that temperature rather than size has been shown to be a decisive factor in affecting the final shape of gold nanoparticles.⁶¹ A number of simple expressions have been used here to describe the temperature dependence of γ_{xi} , which was calculated above at $T = 0$. First, we have used a semiempirical expression for determining of $\gamma(T)$ proposed by Guggenheim,^{62,63}

$$\gamma(T) = \gamma(0) \left(1 - \frac{T}{T_c}\right)^n \quad (6)$$

where n is an empirical parameter (known to be unity for metals⁶⁴) and T_c is the critical temperature at which the structure of the surface deteriorates or changes significantly from the structure in the bulk.⁶⁵ This is known to be 1064.33 °C for the {111} surfaces and 897 °C for {100} surface.⁶⁶ The value of T_c is usually taken as the bulk surface melting temperature, but since this has been shown to be size dependent,³⁵ we have also employed the expression of Qi and Wang⁶⁷

$$T_c = T_m \left(1 - \frac{6\alpha r}{D}\right) \quad (7)$$

where T_m is the macroscopic surface melting temperatures, D is the diameter of the particle, r is the atomic radius, and α is a shape dependent factor defined as the ratio of the surface area of the particle divided by the surface area of a sphere of equivalent volume.⁶⁷ In the present context the temperature dependence of σ_{xi} has been described in the same way.

Using these formulas $\gamma_{xi}(T)$ and $\sigma_{xi}(T)$ may be calculated and the shape of gold nanoparticles investigated via optimization of the ratio **B/A** for a given temperature range. Equation 7 also has the added advantage of introducing another degree of shape dependence,⁶⁷ the effect of which will be to create a feedback loop during the optimization. The optimization of the nanoparticle shape at a given temperature will change T_c , which then affects the temperature dependence in eq 6, which then in turn further alters the shape.

The optimization procedure has been performed at 5 °C intervals of T in the range 300–1300 °C, for a number of nanoparticle sizes. The collective results predict not only the size dependent melting of the particles, in agreement with

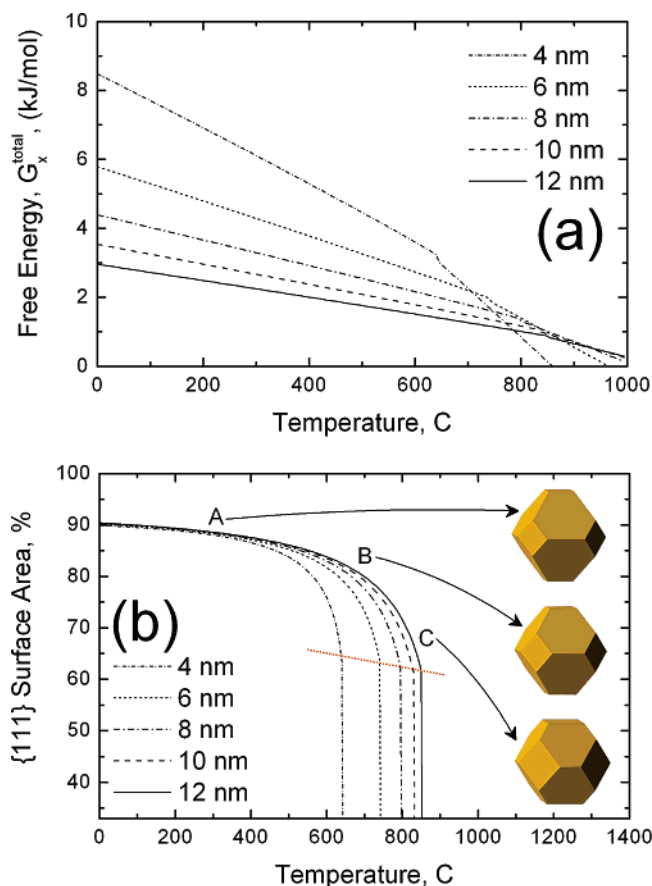


Figure 5. The calculated change in total free energy (a) and fraction of {111} surface area (b) as a function of temperature for 4, 6, 8, 10, and 12 nm gold nanoparticles. The onset of melting is indicated by the abrupt change in the slopes in (a) and by the dotted line bisecting the plots in (b). The shape transition (from truncated octahedron illustrated for point A to a more cuboctahedral morphology as illustrated for point C) is predicted prior to the onset of melting.

experiment, but also that the melting will be preceded by a significant change in nanoparticle morphology. Figure 5a gives the change in G_x^{total} as a function of temperature. For each of the nanoparticle sizes examined, the onset of melting is evident, indicated by the abrupt changes in the slopes. The onset of melting shifts to higher temperatures as the nanoparticle size increases, and the slopes diminish as the particle melting temperature approaches the bulk melting temperature. The corresponding change in nanoparticle shape is illustrated in Figure 5b where the fraction of {111} surface area is plotted as a function of temperature for each particle size. Here again, the onset of melting is shown (by the dotted line bisecting the plots) following a smooth decrease in the {111} surface area (equating to an increase in the {100} surface area) or, equivalently, an increase in truncation of the underlying {111} octahedron. In short, the melting is preceded by a shape transition from a truncated octahedron to a more cuboctahedral-like nanoparticle. (Superficially, the latter of morphology can appear more “spherical” in cross section when viewed from different perspectives.) Given that the shape matching study indicated that the gold nanoparticles (such as those shown in Figure 1) exhibit approximately 77% {111} surface area, we can estimate that these particles have been annealed to $\sim 800^\circ\text{C}$ by the electron beam.

These results are in good agreement with previously reported computational studies examining the melting temperature and thermal stability of unsupported fcc gold nanoparticles.^{68,69} For example, the thermal stability of unsupported nanoparticles

containing 140–6708 atoms, was investigated by Shim and colleagues using molecular dynamics simulation in combination with the modified embedded-atom-method potential.⁶⁸ Their results showed that the melting temperature of the gold nanoparticles decreases drastically with decreasing particle size and that the a premelting phenomenon involving the “disordering” of the surface atoms was observed (prior to the melting of the whole particle).⁶⁸ The melting temperatures for various particle sizes listed in the paper are in excellent quantitative agreement with the results presented here. In a further study of the crystallization of a 4 nm gold particle (upon cooling), the same authors found that with decreasing cooling rate, the final structure of the nanoparticle changes from amorphous to crystalline (via an icosahedron-like structure). Their study concluded that fcc is energetically the most stable structure of the gold nanoparticle at large sizes.⁶⁹ Similarly, the results of Baletto et al. comparing the total energy for ideal icosahedral, decahedral, and truncated octahedral fcc gold nanoparticles up to 40 000 atoms (using semiempirical potentials) also predict the fcc structure will dominate at sizes >500 atoms.²⁵

In general, however, many molecular dynamics simulations have shown that smaller fcc gold nanoparticles transform into Mackay icosahedrons prior to melting. It was found that upon heating small fcc truncated octahedrons and truncated decahedrons underwent a transformation to the icosahedral structure by Cleveland et al.⁷¹ Later, the transformation to an icosahedral motif during simulated freezing of gold nanoparticles up to almost 4000 atoms was also examined by Chushak and Bartell,⁷⁰ and more recently, Wang et al.²⁶ conducted similar molecular dynamic simulations showing that gold clusters between 600 and 3000 atoms crystallize into an icosahedron upon cooling from the liquid phase. In this study the surface facets of the icosahedral clusters were shown to “soften”, due to the increasing mobility of vertex and edge atoms with temperature. This led to interlayer and intralayer diffusion, shrinkage of the average facet size, and eventually to the change to a nearly spherical shape upon melting.²⁶

The importance of size dependence to these results (showing a preference for gold to adopt an icosahedral motif prior to melting) was put into context in a recent study by Kuo and Clancy.²⁷ As part of their own molecular dynamics study of the melting and freezing of supported and unsupported 2–5 nm particles (which also showed the structural transformation from the fcc to an icosahedral at elevated temperature), they found that large fcc particles transformed into a quasi-melting phase (before completely melting). In this region of the phase map, the high values of N , the fcc particles were found to bypass the icosahedral phase all together. They presented a T – N phase map, illustrating the relationship between phases for a given number of atoms (N). In our study, the particle size of interest (chosen to match the nanoparticles shown in Figure 1) will contain $\sim 15\,000$ atoms, and will fall within the *high- N* region of this phase map,²⁷ as can be discerned by examining the precursor to this phase map proposed by Marks.¹⁷

Further, in the case of smaller nanoparticles, a direct route for the conversion of cuboctahedral nanoparticles to icosahedral nanoparticles has been identified,²¹ but no direct path has been found for a truncated octahedron to convert to an icosahedron. It is therefore entirely plausible to suppose that the truncated octahedron to cuboctahedron transition shown herein provides a preliminary step in the melting transitions, which will be subsequently followed by the cuboctahedron to icosahedron transition described in ref 21.

5. Conclusion

In summary, we have systematically investigated the morphology of fcc gold nanoparticles greater than 3 nm in size, using a shape-dependent thermodynamic model combined with surface energies and surface stresses calculated using first principles methods (with relativistic corrections). This is the first time that a study of gold nanoparticle morphology in this size regime has been undertaken using such a high level of theory. The results have shown that among the geometrically "ideal" shapes considered, the truncated octahedron is by far the most energetically favorable, in excellent agreement with experimental observations. Furthermore, it was found that an octahedral morphology and a truncated cubic morphology (respectively) are expected to be lower in energy than a cuboctahedron.

We have also shown, by optimizing the shape of the gold nanoparticles with respect to size, that the equilibrium shape of small fcc gold nanoparticles (less than 20 nm) deviates slightly from that expected from the (macroscopic) Wulff construction. The evolution of this specific nanoscale morphology is due to the need for small particles to minimize the total surface stress and the total surface-to-volume ratio as well as the total surface energy.

The same optimization procedure was used to examine the equilibrium nanomorphology of gold nanoparticles (of various sizes) as a function of temperature, using an semiempirical relationship between the critical temperature the surface energies and surface stresses. These results predict that a shape transformation will be observed prior to melting, characterized by an increase in the fraction of {100} surface area and the adoption of a more cuboctahedral morphology. This prediction is consistent with results from atomistic computer simulations⁶⁸ and is reasonable in light of experimental observations of gold nanoparticles changing shape when exposed to optical^{59,60} or electron^{13,57,58} irradiation. This type of temperature-induced shape transition could account for the observation of the (otherwise metastable) cuboctahedral morphology often observed in large gold nanoparticles^{13,37} and provides a preliminary step before the transition to an icosahedral²¹ shape in small gold nanoparticles before the melting transition.

Acknowledgment. This work has been supported by the U.S. Department of Energy, Basic Energy Sciences, under Contract W-31-109-ENG-38. Computational resources for this project have been supplied by Argonne National Laboratory—Laboratory Computing Resource Center, the MSCF in EMSL (a national scientific user facility sponsored by the U.S. DOE, OBER and located at PNNL), and the U.S. Department of Energy National Energy Research Scientific Computing Center.

References and Notes

- Halperin, W. P. *Rev. Mod. Phys.* **1966**, *38*, 533.
- El-Sayed, M. *Acc. Chem. Res.* **2001**, *34*, 257.
- de Heer, W. *Rev. Mod. Phys.* **1993**, *65*, 611.
- Jensen, P. *Rev. Mod. Phys.* **1999**, *71*, 1695.
- Moriarty, P. *Rep. Prog. Phys.* **2001**, *64*, 297.
- Schiffrin, D. J. *MRS Bull.* **2001**, *26*, 1019. Kreibitz, U.; Vollmer, M. *Optical Properties of Metal Clusters*; Springer-Verlag: Berlin, 1995.
- Wang, Z. L. *J. Phys. Chem. B* **2000**, *104*, 1145.
- Liu, M. Z.; Guyot-Sionnest, P. *J. Phys. Chem. B* **2004**, *108*, 5882.
- Wang, D.-S.; Kerker, M. *Phys. Rev. B* **1981**, *24*, 1777.
- Nikoobakht, B.; Wang, J.; El-Sayed, M. A. *Chem. Phys. Lett.* **2002**, *366*, 17.
- Jana, N. R.; Gearheart, L.; Murphy, C. J. *J. Phys. Chem. B* **2001**, *105*, 4065.
- Chen, S.; Wang, Z. L.; Ballato, J.; Foulger, S. H.; Carroll, D. L. *J. Am. Chem. Soc.* **2003**, *125*, 16186.
- Bovin, J.-O.; Malm, J.-O. *Z. Phys. D* **1991**, *19*, 293. Hou, M. *Phys. Rev. B* **2000**, *62*, 10383.
- Pinto, A.; Pennisi, A. R.; Faraci, G.; D'Agostino, G.; Mobilio, S.; Boscherini, F. *Phys. Rev. B* **1995**, *51*, 5315.
- Buffat, P.-A.; Flüeli, M.; Spycher, R.; Stadelmann, P.; Borel, J.-P. *Faraday Discuss.* **1991**, *92*, 173.
- José-Yacamán, M.; Herrera, R.; Gómez, A. G.; Tehuacanero, S.; Schabes-Retchkiman, P. *Surf. Sci.* **1990**, *237*, 248.
- Marks, L. D. *Rep. Prog. Phys.* **1994**, *57*, 603.
- Martin, T. P. *Phys. Rep.* **1996**, *273*, 199.
- Ascencio, J. A.; Gutiérrez-Wing, C.; Espinosa, M. E.; Marin, M.; Tehuacanero, S.; Zorrilla, C.; José-Yacamán, M. *Surf. Sci.* **1998**, *396*, 349.
- Ascencio, J. A.; Perez, M.; José-Yacamán, M. *Surf. Sci.* **2000**, *447*, 73.
- Aragón, J. L. *Chem. Phys. Lett.* **1994**, *226*, 263.
- Cleveland, C. L.; Landman, U.; Schaaff, T. G.; Shafigullin, M. N.; Stephens, P. W.; Whetten, R. L. *Phys. Rev. Lett.* **1997**, *79*, 1873.
- Cleveland, C.; Luedtke, W. D.; Landman, U. *Phys. Rev. Lett.* **1998**, *81*, 2036.
- Nam, H.-S.; Hwang, N. M.; Yu, B. D.; Yoon, J.-K. *Phys. Rev. Lett.* **2002**, *89*, 275502.
- Baletto, F.; Ferrando, R.; Fortunelli, A.; Montalenti, F.; Mottet, C. *J. Chem. Phys.* **2005**, *122*, 214722.
- Wang, Y.; Teitel, S.; Dellango, C. *J. Chem. Phys.* **2005**, *122*, 214722.
- Kuo, C.-L.; Clancy, P. J. *J. Phys. Chem. B* **2005**, *109*, 13743.
- Baletto, F.; Ferrando, R. *Rev. Mod. Phys.* **2005**, *77*, 371.
- Whetten, R. L.; Khoury, J. T.; Alvarez, M. M.; Murthy, S.; Vezmar, I.; Wang, Z. L.; Stephens, P. W.; Cleveland, C. L.; Luedtke, W. D.; Landman, U. *Adv. Mater.* **1996**, *8*, 428.
- Pauwels, B.; Van Tendeloo, G.; Bouwen, W.; Theil Kuhn, L.; Lievens, P.; Lei, H.
- Baletto, F.; Mottet, C.; Ferrando, R. *Chem. Phys. Lett.* **2002**, *354*, 82.
- Koga, K.; Sugawara *Surf. Sci.* **2003**, *529*, 23.
- Barnard, A. S.; Zapol, P. *J. Chem. Phys.* **2004**, *121*, 4276.
- Barnard, A. S.; Curtiss, L. A. *Rev. Adv. Mater. Sci.* **2005**, *10*, 105.
- Buffat, Ph.; Borel, J.-P. *Phys. Rev. A* **1976**, *13*, 2287.
- Lin, X.-M.; Sorensen, C. M.; Klabunde, K. J. *J. Nanopart. Res.* **2000**, *2*, 157.
- Page, K.; Proffen, T.; Terrones, H.; Terrones, M.; Lee, L.; Yang, Y.; Stemmer, S.; Seshadri, R.; Cheetham, A. K. *Chem. Phys. Lett.* **2004**, *393*, 385.
- Bilić, A.; Reimers, J. R.; Hush, N. S.; Hafner, J. *J. Chem. Phys.* **2002**, *116*, 8981.
- Kollár, J.; Vitos, L.; Osorio-Guillén, J. M.; Ahuja, R. *Phys. Rev. B* **2003**, *68*, 245417.
- Vinet, P.; Rose, J. H.; Ferrante, J.; Smith, J. R. *J. Phys.: Condens. Matter* **1989**, *1*, 1941.
- Heinz, D. L.; Jeanloz, R. *J. Appl. Phys.* **1984**, *55*, 885.
- Holzapfel, W.; Hartwig, M.; Sievers, W. *J. Phys. Chem. Ref. Data* **2001**, *30*, 515.
- Perdew, J.; Wang, Y. *Phys. Rev. B* **1992**, *45*, 13244.
- Kresse, G.; Hafner, J. *Phys. Rev. B* **1993**, *47*, RC558.
- Kresse, G.; Hafner, J. *Phys. Rev. B* **1996**, *54*, 11169.
- Kresse, G.; Furthmüller, J. *Comput. Mater. Sci.* **1996**, *6*, 15.
- Wood, D. M.; Zunger, A. *J. Phys. A* **1985**, *18*, 1343.
- Blöchl, P. E. *Phys. Rev. B* **1994**, *50*, 17953.
- Kresse, G.; Joubert, D. *Phys. Rev. B* **1999**, *59*, 1758.
- Vosko, S. H.; Wilk, L.; Nusair, M. *Can. J. Phys.* **1980**, *58*, 1200.
- Needs, R. J.; Mansfield, M. *J. Phys.: Condens. Matter* **1989**, *1*, 7555.
- Vitos, L.; Ruban, A. V.; Skriver, H. L.; Kollár, J. *Surf. Sci.* **1998**, *411*, 186.
- Galanakis, I.; Bihlmayer, G.; Bellini, V.; Papanikolaou, N.; Zeller, R.; Blügel, S.; Dederichs, P. H. *Europhys. Lett.* **2002**, *58*, 751.
- Solliard, C.; Flüeli, M. *Surf. Sci.* **1985**, *156*, 487.
- Flüeli, M.; Borel, J.-P. *J. Cryst. Growth* **1998**, *91*, 67.
- Wulff, G. *Z. Kristallogr. Mineral.* **1901**, *34*, 449.
- Iijima, S.; Ichihashi, T. *Phys. Rev. Lett.* **1986**, *56*, 616.
- Ben-David, T.; Lereah, Y.; Deutscher, G.; Penisson, J. M.; Bourret, A.; Kofman, R.; Cheyssac, P. *Phys. Rev. Lett.* **1997**, *78*, 2585.
- Link, S.; Burda, C.; Nikoobakht, B.; El-Sayed, M. A. *J. Phys. Chem. B* **2000**, *104*, 6152.
- Inasawa, S.; Sugiyama, M.; Yamaguchi, Y. *J. Phys. Chem. B* **2005**, *109*, 3104.
- Büttner, M.; Belser, T.; Oelhafen, P. *J. Phys. Chem. B* **2005**, *109*, 5464.
- Guggenheim, E. A. *J. Chem. Phys.* **1945**, *13*, 253.
- Guggenheim, E. A. *Thermodynamics*, 4th ed.; North-Holland: Amsterdam, 1993.
- Grosse, A. V. *J. Inorg. Nucl. Chem.* **1962**, *24*, 147.
- Somorjai, G. A. *Introduction to surface chemistry and catalysis*; John Wiley & Sons: New York, 1994.

- (66) Mochrie, S. G. J.; Zehner, D. M.; Ocko, B. M.; Gibbs, D. *Phys. Rev. Lett.* **1990**, *64*, 2925. Gibbs, D.; Ocko, B. M.; Zehner, D. M.; Mochrie, S. G. J. *Phys. Rev. B* **1992**, *42*, 7330; *Phys. Rev. B* **1988**, *38*, 7303.
- (67) Qi, W. H.; Wang, M. P. *Mater. Chem. Phys.* **2004**, *88*, 280.
- (68) Shim, J.-H.; Lee, B.-J.; Cho, Y. W. *Surf. Sci.* **2002**, *512*, 262.
- (69) Shim, J.-H.; Lee, S.-C.; Lee, B.-J.; Suh, J.-Y.; Cho, Y. W. *J. Cryst. Growth* **2003**, *250*, 558.
- (70) Chushak, Y. G.; Bartell, L. S. *J. Phys. Chem. B* **2001**, *105*, 605.
- (71) Cleveland, C.; Luedtke, W. D.; Landman, U. *Phys. Rev. B* **1999**, *60*, 5065.